Effect of Ti substitution for Al on the cuboidal nanoprecipitates in $Al_{0.7}NiCoFeCr_2$ high-entropy alloys

Chunling Li, Yue Ma, Jiamiao Hao, and Qing Wang[a)]
Key Laboratory of Materials Modification by Laser, Ion and Electron Beams (Ministry of Education), School of Materials Science and Engineering, Dalian University of Technology, Dalian 116024, China

Shujie Pang
Key Laboratory of Aerospace Materials and Performance (Ministry of Education), School of Materials Science and Engineering, Beihang University, Beijing 100191, China

Chuang Dong
Key Laboratory of Materials Modification by Laser, Ion and Electron Beams (Ministry of Education), School of Materials Science and Engineering, Dalian University of Technology, Dalian 116024, China

Peter K. Liaw[b)]
Department of Materials Science and Engineering, The University of Tennessee, Knoxville, Tennessee 37996, USA

(Received 16 March 2018; accepted 11 June 2018)

Coherent cuboidal B2 nanoprecipitation in body-centered cubic (BCC)-based high-entropy alloys (HEAs) is important for the improvement of mechanical strength. The present work primarily investigated the effect of Ti substitution for Al on the cuboidal B2 nanoprecipitates in BCC $Al_{0.7}NiCoFeCr_2$ HEAs. A series of $(Al,Ti)_{0.7}NiCoFeCr_2$ HEAs with different Al/Ti ratios were prepared by suction-cast processing, and their microstructures and mechanical properties were then characterized comprehensively. It was found that the substitution of Ti for Al can change the phase structures of ordered precipitation, from the B2-AlNi to a highly ordered $L2_1$-Ni_2AlTi phase. Especially, a small amount addition of Ti ($\leq$4.2 at.%, Al/Ti ratio $\geq$2/1) renders the HEAs with cuboidal $L2_1$ nanoparticles coherently precipitated into the BCC matrix, which is attributed to the moderate lattice misfit (ε = 0.5–0.6%) between BCC and $L2_1$ phases. HEAs with such coherent microstructures exhibit high compressive yield strength of about 1700–1800 MPa. When the Ti content reaches up to 6.25 at.%, the matrix of the alloy will be turned into the σ phase, rather than BCC, leading to a heavy brittleness.

I. INTRODUCTION

Recently, high-entropy alloys (HEAs) have attracted more attention due to their unique properties caused by simple crystalline structures and multiple-component mixing.[1–5] They generally possess simple crystalline structures, such as face-centered-cubic (FCC),[6,7] body-centered-cubic (BCC),[8–10] and hexagonal close-packed (HCP) solid solution structures.[11–13] For instance, the single-phase FCC CoCrFeNiMn (in equimolar fraction) HEA displays outstanding damage tolerance with higher tensile strength and fracture toughness than traditional engineering stainless steels at cryogenic temperatures.[6] Refractory high-entropy alloys with a single-phase BCC structure exhibit good oxidation- and corrosion-resistances at high temperatures (HTs) besides their high strengths.[8–10] To further improve the strength of HEAs, some kinds of intermetallic compounds, such as Laves phase and coherent ordered phases ($L1_2$-Ni_3Al, B2-NiAl, and $L2_1$-Ni_2AlTi), are expected to be precipitated in the FCC or BCC solid solution matrix.[14–17]

High strength and good ductility of engineering alloys at elevated temperatures are mainly dependent on the morphologies (shape and size) and distribution of precipitates.[18,19] Specially, the coherent precipitation of cuboidal $L1_2$-Ni_3Al nanoparticles from the parent FCC matrix is expected in Ni-based superalloys since this kind of microstructure can contribute to the prominent high-temperature creep-resistant properties.[20,21] Such a phenomenon also occurred in HEAs.[15,22,23] The dispersion of spherical $L1_2$-$Ni_3(Al,Ti)$ nanoparticles in the FCC matrix renders the $(FeCoNiCr)_{94}Al_4Ti_2$ (at.%) HEA with high strength and good ductility.[15,22] Similarly, the BCC $Al_{0.7}NiCoFe_2Cr$ HEA possesses an excellent combination of higher strength and good ductility at room- and elevated-temperatures, which is resulted from the coherent precipitation of cuboidal B2 nanoparticles in the BCC matrix.[23]

It is difficult to achieve cuboidal or spherical shapes of coherent B2 precipitates in BCC-based HEAs due to the

a)Address all correspondence to this author.
e-mail: wangq@dlut.edu.cn
b)This author was an editor of this journal during the review and decision stage. For the *JMR* policy on review and publication of manuscripts authored by editors, please refer to http://www.mrs.org/editor-manuscripts/.
DOI: 10.1557/jmr.2018.213

large composition difference between BCC and B2 phases that can induce a large lattice misfit.[24] The weave-like microstructure caused by spinodal decomposition between these two phases is always existed in BCC/B2 Al-contained HEAs, like AlNiCoFeCr,[25,26] resulting in a serious brittleness. Further addition of a small amount of Ti into $AlNiCoFeCrTi_x$ ($x < 0.5$, Ti < 9.1 at.%) HEAs does not change the morphology of alloys, still keeping the spinodal decomposition of BCC and B2 phases.[27,28] However, a large amount of Ti addition (16.7–23 at.%) in this HEA series could change the phase constitutions, in which the $L2_1$-Ni_2AlTi and Fe_2Ti-type Laves phases replaced the B2 to be as the secondary strengthening phases on the BCC matrix.[28,29] It was noted that the precipitation of the Fe_2Ti phase in the BCC-based $AlNiCoFeCrTi_{1.5}$ HEA reduced the plasticity seriously although the strength was enhanced.[28] Occasionally, there also exist other kinds of brittle phases, such as chi-phase (cI-Mn type), R-phase (hR-Ni_2Ti type), σ phase (tP-CrFe type), etc., all of which will deteriorate mechanical properties of HEAs.[30,31]

It was found that the coherent spherical B2 nanoprecipitation in the BCC matrix of the Fe–10Cr–10Ni–6.5Al–3.4Mo (in weight percent, wt%) ferritic steel, designated as the FBB8 alloy, can enhance the mechanical properties at both room- and high-temperatures.[32,33] Intriguingly, further addition of 2 wt% Ti into FBB8 renders the alloy with cuboidal $L2_1$/B2 hierarchical nanoprecipitates, resulting in a significant improvement of the creep-resistant property at a HT of 700 °C.[33–36] In addition, cuboidal $L2_1$ nanoparticles were also precipitated in a newly designed light-weight BCC-based $Al_{1.5}CrFeMnTi$ HEA, which exhibits a high microstructural stability.[37] In our recent work, we designed a series of HEAs[23,38] with a composition of Al_2M_{14} (M represents different combinations of Ni, Co, Fe, and Cr) with the guide of the cluster formula approach,[39] in which the cuboidal B2 nanoparticles are found to be precipitated coherently into the BCC matrix.[23,38] Among them, the typical BCC $Al_{0.7}NiCoFeCr_2$ HEA, derived from the composition of Al_2M_{14} with $M = Ni_1Co_1Fe_1Cr_2$, exhibits a higher yield strength of above 1700 MPa due to the special coherent microstructure.[38] Similar to Al, Ti also interacts strongly with Ni, Co, Fe, and Cr, which can be characterized by the enthalpy of mixing, ΔH, between Al and Ti with these transition metals.[40] Actually, the influence of Ti, as a replacer of Al, on the microstructure of HEAs has seldom been reported. Therefore, the present work will aim primarily at investigating the phase constitution and particle morphology in $(Al,Ti)_{0.7}NiCoFeCr_2$ HEAs by the Ti substitution for Al, in which the Al/Ti ratios are changed, while the combination of transition metals is fixed. The microstructure evolution induced by the Ti substitution for Al in this HEA series will be discussed from the viewpoint of the lattice misfit between the coherent phases and matrix. The mechanical properties of the designed HEAs will also be discussed.

II. EXPERIMENTAL

Four alloys of $(Al,Ti)_{0.7}NiCoFeCr_2$ with different Al/Ti ratios were prepared by means of arc melting and suction cast into a 3 mm-diameter cylindrical copper mold under an argon atmosphere. Purities of the raw elemental metals are 99.99% for Al, Ti, Co, Fe, and Ni, and 99.9% for Cr. Mixtures of raw materials with appropriate compositions and a total weight of about 5 g were remelted at least five times to ensure the chemical homogeneity before suction casting. The basic $Al_{0.7}NiCoFeCr_2$ alloy without Ti is denoted as T0, and the alloys with different Al/Ti ratios of 3/1, 2/1, and 1/1 are denoted as T1, T2, and T3, respectively. Table I lists the chemical compositions in atomic percent (at.%) of these designed HEAs.

The crystalline structures of these as-cast alloys were identified, using a Bruker D8 X-ray diffractometer (XRD; Bruker, Ettlingen, Germany) with a Cu K_α radiation ($\lambda = 0.15406$ nm) and a scanning speed of 2°/min, in which an external standard method was applied to calculate the lattice constants of phases.[41] The microstructure was examined using an Olympus optical microscope (OM; Olympus Corporation, Tokyo, Japan), Zeiss Supra 55 scanning electron microscope (SEM; Carl Zeiss, Oberkochen, Germany), and JEOL-JEM-2100F field emission transmission

TABLE I. Data summary for the designed HEAs with different Ti contents, including nominal formula and compositions in atomic percent, phase constitutions and their volume fraction (f), lattice constant (a), lattice misfit (ε), average particle size (r) of $L2_1$ and B2 phases, compressive yield strength (σ_y), and microhardness (HV).

No.	Nominal formula (composition in at.%)	Phase constitution (f, %)	a (nm)	ε (%)	r (nm)	σ_y (MPa)	HV
T0	$Al_{0.7}NiCoFeCr_2$ ($Al_{12.5}Ni_{17.5}Co_{17.5}Fe_{17.5}Cr_{35}$)	BCC + B2 (~55%)	$a_{BCC} = 0.2856 \pm 0.0003$ $a_{B2} = 0.2869 \pm 0.0006$	0.45 ± 0.11	100 ± 20	1705 ± 34	626 ± 6
T1	$(Al_3Ti)_{0.7}NiCoFeCr_2$ ($Al_{9.4}Ti_{3.1}Ni_{17.5}Co_{17.5}Fe_{17.5}Cr_{35}$)	BCC + $L2_1$ (~46%)	$a_{BCC} = 0.2875 \pm 0.0002$ $a_{L21} = 0.5781 \pm 0.0003$	0.54 ± 0.12	80 ± 10	1791 ± 18	641 ± 6
T2	$(Al_2Ti)_{0.7}NiCoFeCr_2$ ($Al_{8.3}Ti_{4.2}Ni_{17.5}Co_{17.5}Fe_{17.5}Cr_{35}$)	BCC + $L2_1$ (~49%)	$a_{BCC} = 0.2893 \pm 0.0002$ $a_{L21} = 0.5824 \pm 0.0002$	0.65 ± 0.10	55 ± 5	1826 ± 42	634 ± 7
T3	$(AlTi)_{0.7}NiCoFeCr_2$ ($Al_{6.25}Ti_{6.25}Ni_{17.5}Co_{17.5}Fe_{17.5}Cr_{35}$)	σ + $L2_1$ + BCC	$a_\sigma = 0.8817 \pm 0.0006$ $c_\sigma = 0.4562 \pm 0.0004$	...	...	...	924 ± 6

electron microscope (TEM; JEOL Ltd., Tokyo, Japan) equipped with a JEM2100F FEG scanning transmission electron microscope (STEM; JEOL Ltd., Tokyo, Japan). The etching solution used for the sample preparation for OM and SEM observations contains 5 g $FeCl_3 \cdot 6H_2O$ + 25 mL HCl + 25 mL C_2H_5OH, and the TEM samples were prepared by twin-jet electropolishing in a solution of 10% $HClO_4$ + 90% C_2H_5OH (volume fraction) at a cryogenic temperature of −30 °C. Statistical analysis on the volume fraction and the particle size of BCC, B2, and $L2_1$ phases were performed with at least 3 SEM or TEM morphology images. The elemental distributions and chemical compositions in different regions of HEAs were analyzed by using a SHIMADZU electron probe micro-analyzer (EPMA; Shimadzu, Kyoto, Japan).

The uniaxial compressive tests were conducted on an 810 Material Test System (MTS, Cary, North Carolina) at a nominal strain rate of 2×10^{-3}/s at room temperature. The machine stiffness was first evaluated to compensate the true strain. It was measured by compressing a same-size 310S stainless steel sample with a known Young's modulus of 205 GPa, from which the force–displacement curve was obtained, and the machine stiffness was deduced after subtracting the elastic contribution from the 310S sample. The measured machine stiffness was subsequently integrated in the compressive strain to properly convert the engineering compression to true compression. At least three cylindrical specimens with a size of ϕ 3 × 6 mm were tested for each alloy. Values of microhardness of HEAs were measured using a HVS-1000 Vickers hardness tester under a constant load of 500 g for 20 s, and at least 12 indents were taken.

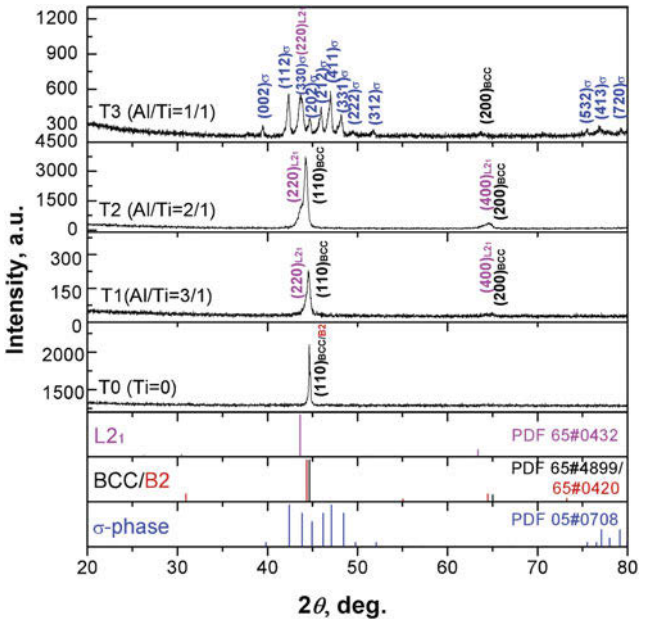

FIG. 1. XRD patterns of the designed HEAs with different Ti contents.

III. RESULTS

A. Microstructural characteristics

The XRD patterns for the designed as-cast HEAs are shown in Fig. 1, in which the basic $Al_{0.7}NiCoFeCr_2$ HEA without Ti (T0) exhibits a single BCC/B2 phase, since it contains a much more amount of BCC-stabilizers (Fe and Cr).[38] The substitutions of Ti for Al in T1 (Al/Ti = 3/1) and T2 (Al/Ti = 2/1) alloys widen the primary diffraction peaks of (110) and (200) of the BCC phase strongly,

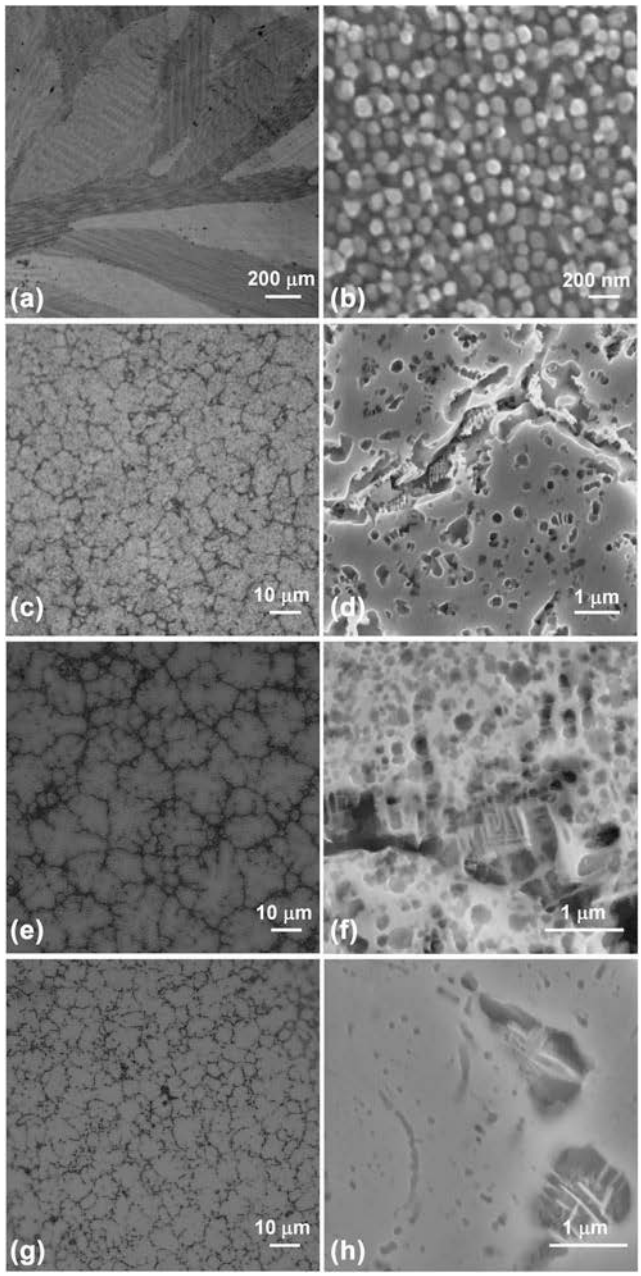

FIG. 2. OM and SEM micrographs of HEAs: (a) and (b) for the basic $Al_{0.7}NiCoFeCr_2$ alloy without Ti (T0); (c) and (d) for the alloy with an Al/Ti ratio of 3/1 (T1); (e) and (f) for the alloy with an Al/Ti ratio of 2/1 (T2); (g) and (h) for the alloy with an Al/Ti ratio of 1/1 (T3).

which is resulted from the precipitation of the coherent $L2_1$-Ni_2AlTi phase (a highly ordered superstructure of BCC). That is to say, a certain amount of Ti addition can induce a phase transition from the ordered B2 to a highly ordered $L2_1$ phase in BCC-based HEAs. However, the further substitution of Ti (6.25 at.%) for Al changes the structure of the matrix from the BCC to a σ phase with a tetragonal structure in the T3 alloy with a Al/Ti ratio of 1/1, besides the $L2_1$ precipitation. The lattice constants of the phases in these HEAs were also measured and are listed in Table I. Moreover, the morphological variations in this HEA series were confirmed by OM and SEM observations, as shown in Fig. 2. The basic T0 alloy is composed of coarse columnar dendrites [Fig. 2(a)], in which a large amount of cuboidal B2 nanoparticles (with a size of 80–120 nm) are coherently precipitated in the BCC matrix [Fig. 2(b)].[38] While the substitutions of Ti for Al render the alloys (T1–T3) with fine equiaxed dendrites [Figs. 2(c), 2(e), and 2(g)], and with a weave-like microstructure composed of BCC and $L2_1$ in the interdendritic regions [Figs. 2(d), 2(f), and 2(h)]. It is noted that a similar morphology of cuboidal $L2_1$ nanoparticles appears in the BCC inner-dendrites in T1 and T2 alloys. Although the T3 alloy is still constituted of fine equiaxed dendrites, it does not show the BCC structure, but the σ. It was also demonstrated by the EPMA results (Fig. 3), in which Cr and Fe are enriched in the inner-dendrites, while Al, Ti, and Ni are especially segregated in the interdendrites. The compositions in the inner-dendritic and interdendritic regions are about $Al_{3.8}Ti_{3.5}Ni_{12.5}Co_{16.4}Fe_{19.0}Cr_{44.8}$ and $Al_{15.0}Ti_{13.8}Ni_{25.7}Co_{18.0}Fe_{10.2}Cr_{17.3}$ (at.%), respectively. Obviously, the Cr and Fe contents in inner-dendrites are higher than the values of the nominal composition, $Al_{6.25}Ti_{6.25}Ni_{17.5}Co_{17.5}Fe_{17.5}Cr_{35}$. The total amount of Fe and Co is very close to that of Cr, indicating that the matrix structure has transformed into a (Fe,Co)Cr-type σ phase. In addition, the serious segregation of Al and Ti in the interdendrites results in the total amount of (Al + Ti) almost equal to that of Ni, demonstrating that the precipitation phase is $L2_1$-Ni_2AlTi, which is in consistent with the XRD results.

To determine the morphology evolution of nanoprecipitates with Ti alloying, TEM analysis was performed particularly. For the basic T0 HEA, the dark-field (DF)

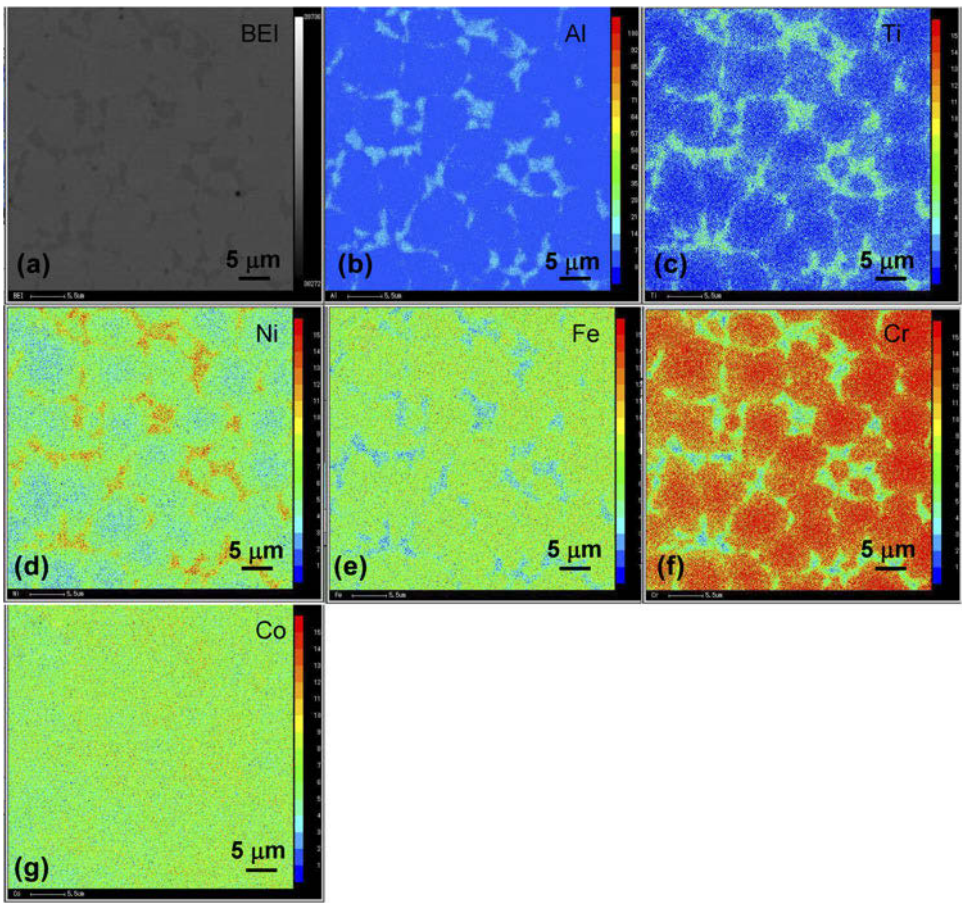

FIG. 3. Elemental distributions of the T3 alloy (Al/Ti = 1/1) mapped by using an EPMA. (a) Backscattered electron image of the T3 alloy; (b–g) elemental distributions of Al, Ti, Ni, Fe, Cr, and Co, respectively.

image and the selected-area electron diffraction (SAED) pattern in Fig. 4(a) verify that it is the cuboidal B2 nanoparticles with a volume fraction of about 55% precipitated coherently in the BCC matrix. Intriguingly, in the T1 HEA with an Al/Ti ratio of 3/1 (3.1 at.% Ti), the representative SAED pattern along $\langle 110 \rangle_{BCC}$ and its corresponding DF image taken from the inner-dendrites demonstrate that the coherent nanoprecipitates still maintain the special cuboidal shape but possess a $L2_1$-Ni_2AlTi structure due to the appearance of the weak diffraction spots of $(1\bar{1}\bar{1})$ and $(1\bar{1}3)$ peculiar to $L2_1$, not B2, in the BCC matrix, as shown in Fig. 4(b). The particle size of the cuboidal $L2_1$ nanoprecipitates is in the range of 70–90 nm, and the volume fraction is about 46%. In addition, the weave-like microstructure in the interdendrites is also composed of the $L2_1$ coherent precipitates with the BCC matrix [Fig. 4(c)]. Further addition of Ti (4.2 at.% Ti) with a ratio of Al/Ti = 2/1 does not change the coherent morphology of $L2_1$ in the T2 alloy, in which the cuboidal $L2_1$ nanoparticles are still precipitated in the BCC matrix with a size of 50–60 nm and a volume fraction of about 49% in the inner-dendrites, as presented in Fig. 4(d). And the weave-like microstructure of BCC/$L2_1$ in the interdendrites is similar to that in T1 [Fig. 2(f)]. It is worth noting that the particle size of cuboidal $L2_1$ nanoprecipitates is gradually reduced with increasing the Ti content, while the volume fraction of $L2_1$ precipitates in the inner-dendrites keeps almost constant.

The high-resolution TEM (HRTEM) images of the T1 HEA are displayed in Fig. 5, in which the interface between the BCC matrix and the cuboidal $L2_1$ nanoprecipitate is marked with a black curve [Fig. 5(a)]. Obviously, there exists only one group of parallel atomic planes on the right side of the interface, as shown in Fig. 5(b). The fast Fourier transformation (FFT) pattern [Fig. 5(c)] taken from the red flame in Fig. 5(a) demonstrates that this group of planes of $(\bar{1}10)$ in one direction belongs to the BCC phase, which are marked with red lines in Fig. 5(b). Distinctly different from the right side, there also exist another two groups of parallel atomic planes, $(1\bar{1}1)$ and $(\bar{1}11)$, on the left side of the interface, respectively marked with purple and yellow lines in Fig. 5(b), which are confirmed to be peculiar to the $L2_1$ by the FFT pattern [Fig. 5(d)].

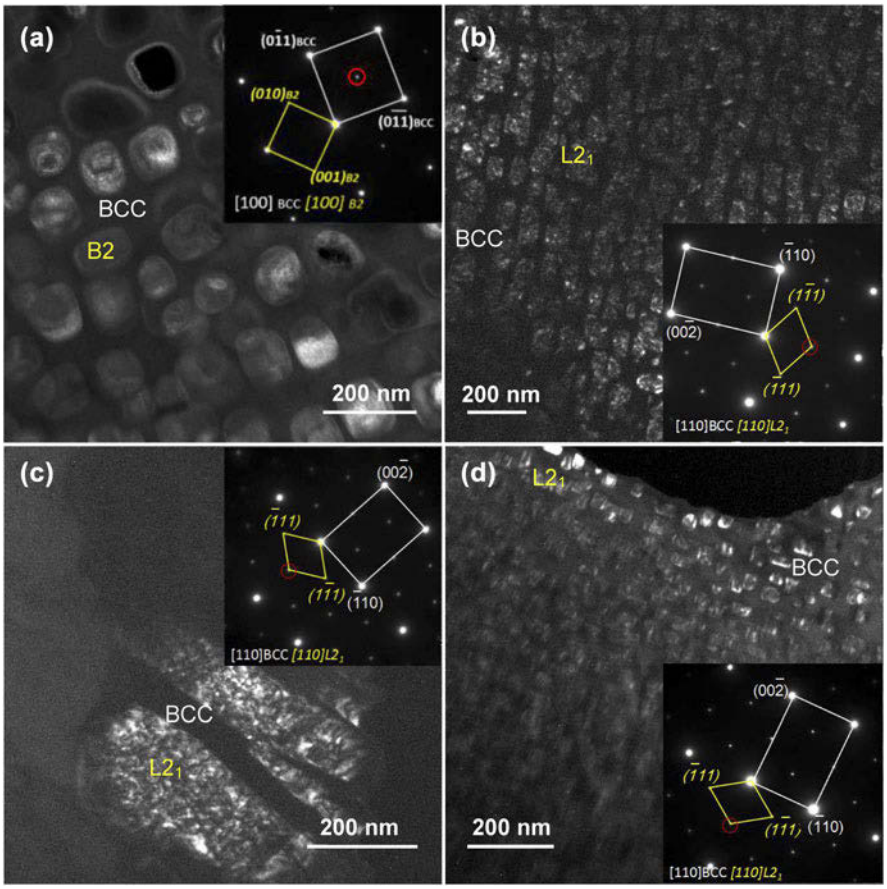

FIG. 4. TEM DF images and corresponding SAED patterns of HEAs. (a) cuboidal B2 nanoparticles embedded coherently into the BCC matrix of the T0 (Ti = 0); (b) cuboidal $L2_1$ nanoprecipitates in the inner-dendrite of the T1 (Al/Ti = 3/1); (c) BCC/$L2_1$ in the interdendrite of the T1; and (d) cuboidal $L2_1$ nanoprecipitates in the inner-dendrite of the T2 (Al/Ti = 2/1).

Moreover, the elemental distribution in the T1 alloy is also analyzed with the STEM, as shown in Fig. 6, in which the selected region is close to the grain boundary of the equiaxed dendrites, including the inner-dendrite and interdendrite. It is found that the Al, Ti, and Ni elements are enriched in both the cuboidal nanoparticles of the inner-dendrite and the plate-like precipitate in the interdendrite. The measured chemical compositions of these two shapes of precipitates are listed in Table II, in which the total amount of (Al + Ti) is approximate to that of Ni, indicating that both are $L2_1$-Ni_2AlTi. Besides, no matter in the inner-dendrites or in the interdendrites, Fe and Cr are mainly segregated in the BCC matrix, while Co is distributed homogeneously in both the BCC matrix and $L2_1$ precipitates.

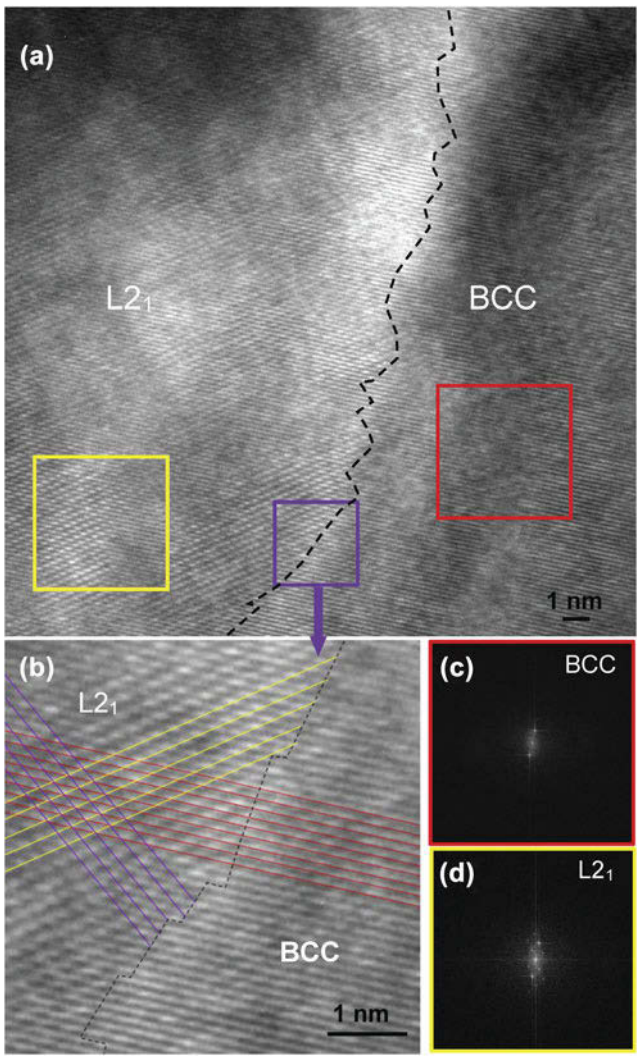

FIG. 5. HRTEM images of the T1 HEA with an Al/Ti ratio of 3/1. (a) HRTEM image showing the interfaces between the BCC matrix and cuboidal $L2_1$ nanoprecipitate; (b) high-magnification HRTEM image caught from (a) showing the details of the BCC/$L2_1$ interface; (c) and (d) FFT patterns of the BCC matrix and $L2_1$ nanoprecipitate, respectively.

B. Mechanical properties

Figure 7 shows the true compressive stress–strain curves of this series of HEAs at room temperature, from which the compressive yield strength (σ_y) is measured and listed in Table I. Compared with the basic T0 alloy with a BCC/B2 microstructure of coarse columnar dendrites, Ti substitution for Al renders the $(Al, Ti)_{0.7}NiCoFeCr_2$ serial alloys (T1 and T2) with fine equiaxed dendrites composed of coherent BCC and $L2_1$ phases, as a result of a further increase in yield strength from ~1700 MPa without Ti to ~1800 MPa with Ti due to the refinement strengthening. The compressive strain values of Ti-added alloys are also higher than that of the basic T0 alloy. More importantly, all these three HEAs exhibit much higher strengths, which is primarily resulted from the coherent microstructure of cuboidal B2 or $L2_1$ nanoprecipitates in the BCC matrix. It has been demonstrated that the coherent strengthening of cuboidal B2-AlNi or $L2_1$-Ni_2AlTi nanoprecipitates in the BCC matrix can improve mechanical property of alloys on a large extent.[23,35,38] Comparing the T1 with the T2 containing similar microstructure but different Ti contents, the latter T2 HEA exhibits a relatively higher strength (1826 ± 42 MPa) than the former T1 (1791 ± 18 MPa), which might be caused by the smaller particle size of $L2_1$ nanoprecipitates. Further increasing the Ti content up to 6.25 at.% in the T3 alloy with an Al/Ti ratio of 1/1, the alloy is brittle and the fracture happens before yielding, which is caused by the brittle σ matrix. Moreover, the microhardness HV of all the designed alloys were measured, from which it is found that the T3 alloy has the highest microhardness with HV = 924, while other alloys have comparable microhardness with a value of about 630.

IV. DISCUSSION

It was known that the ordered B2 phase is always coherent with the BCC parent phase in the Al–Ni–Co–Fe–Cr HEA-forming system due to the strong interactions between Al and these transition metals. Ti addition can induce a phase transformation from an ordered B2-NiAl superstructure to a highly ordered $L2_1$-Ni_2AlTi phase, also named after Heusler phase,[42,43] since Ti also acts strongly with Ni, like Al and Ni. On the other side, the atomic size of Ti is relatively larger than those of Al and Ni, which can result in a large lattice distortion and, thus, induces an ordered phase transformation from B2 to $L2_1$ phase. More importantly, in our recent work,[23,24,38] the formation of a special coherent microstructure with cuboidal B2 nanoprecipitates in BCC HEAs was found to be related closely to the lattice misfit, ε, between B2 and BCC phases, which is expressed with the formula of $\varepsilon = 2 \times (a_{B2} - a_{BCC})/(a_{B2} + a_{BCC})$. Generally, a small ε corresponds to the formation of spherical particles and it is difficult to control the shape of coherent particles in

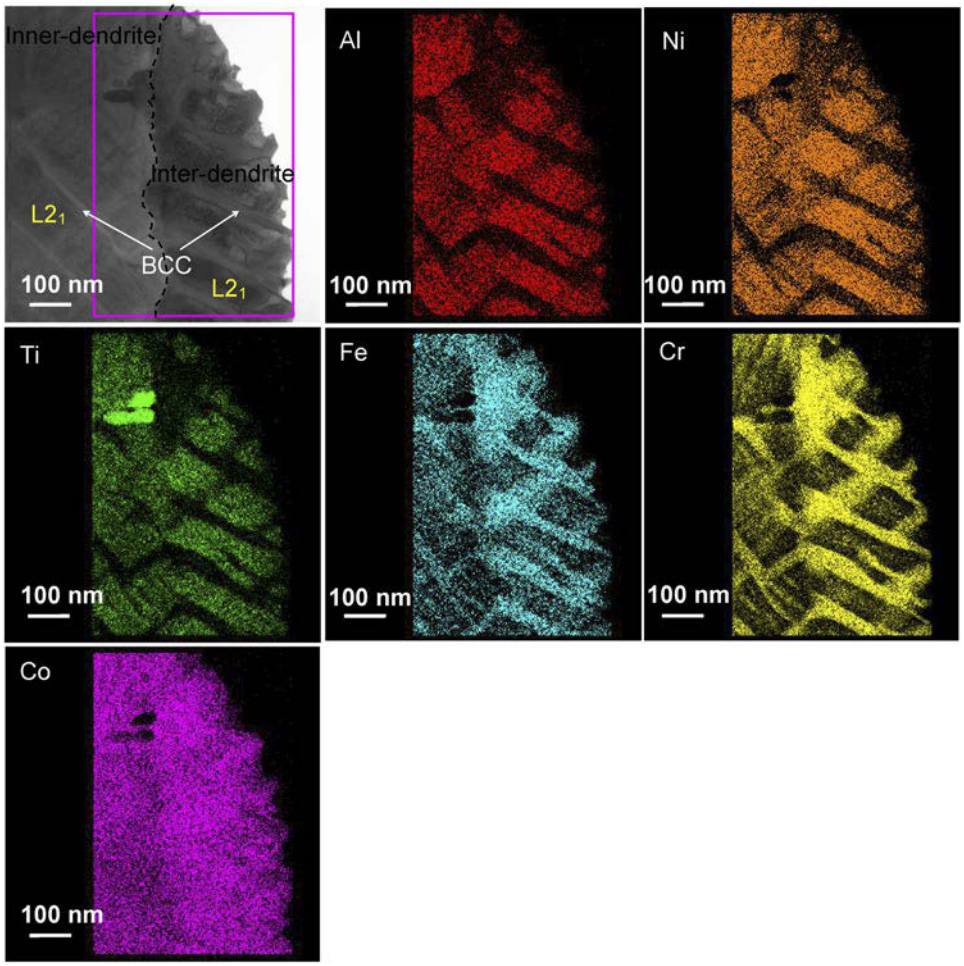

FIG. 6. Elemental distribution of the inner-dendrite and interdendrite of the T1 HEA (Al/Ti = 3/1) mapped with STEM.

TABLE II. Compositions (atomic percent, at.%) of the $L2_1$ precipitates and BCC matrix in different regions of the T1 HEA ($Al_{9.4}Ti_{3.1}Ni_{17.5}Co_{17.5}Fe_{17.5}Cr_{35}$ at.%).

		Al	Ti	Ni	Co	Fe	Cr
	Nominal composition	9.4	3.1	17.5	17.5	17.5	35.0
Dendrites	$L2_1$	24.4	6.5	31.2	17.1	9.9	10.9
	Matrix	3.1	0.7	9.7	17.4	20.7	48.4
Near inter-dendrites	$L2_1$	16.8	8.5	27.9	17.8	11.4	17.6
	Matrix	1.5	0.6	9.3	18.1	22.0	48.5
Inter-dendrites	$L2_1$	19.4	9.9	31.7	18.4	9.9	10.7
	Matrix	1.7	0.5	9.5	18.2	22.0	48.1

the case with a large ε.[44–46] Only a moderate ε can produce such a coherent microstructure with cuboidal particles that contributes to the improvement of high-temperature mechanical properties of alloys, especially the creep-resistant property.[20,21] The cuboidal B2 nanoprecipitates in the T0 alloy are indeed derived from the moderate ε = 0.45%. Although the Ti substitution for Al changes the B2 phase to $L2_1$ phase with a larger lattice constant, nearly twice that of the BCC structure, we also calculated the lattice misfit between BCC and $L2_1$ phases with the formula of $\varepsilon = 2 \times (a_{L2_1} - a_{BCC} \times 2)/(a_{L2_1} + a_{BCC} \times 2)$, as listed in Table I. It is found that the formations of cuboidal $L2_1$ nanoprecipitates in both T1 (Al/Ti = 3/1) and T2 (Al/Ti = 2/1) are all resulted from the moderate lattice misfit, ε = 0.54% for T1 and ε = 0.65% for T2, respectively.

It is necessary to be pointed out that the cuboidal $L2_1$ precipitation in T1 and T2 HEAs occurs in the inner-dendrites alone, while the interdendrites exhibit a weave-like microstructure of $L2_1$ and BCC [Figs. 2(d) and 2(f)]. The chemical compositions of $L2_1$ and BCC phases in different regions of the T1 HEA were measured with the STEM analysis, as listed in Table II. It can be seen that the Ti content in $L2_1$ increases gradually from 6.5 at.% in the inner-dendrites, to 8.5 at.% in the near inner-dendrites, and then to 9.9 at.% in the interdendrites. Since the atomic size of Ti is larger than those of Ni and Al, the increase of Ti content in $L2_1$ will surely cause a relatively larger lattice constant, as a result of the increase of the lattice misfit, ε, between BCC and $L2_1$ phases. We roughly calculated the lattice constants of $L2_1$

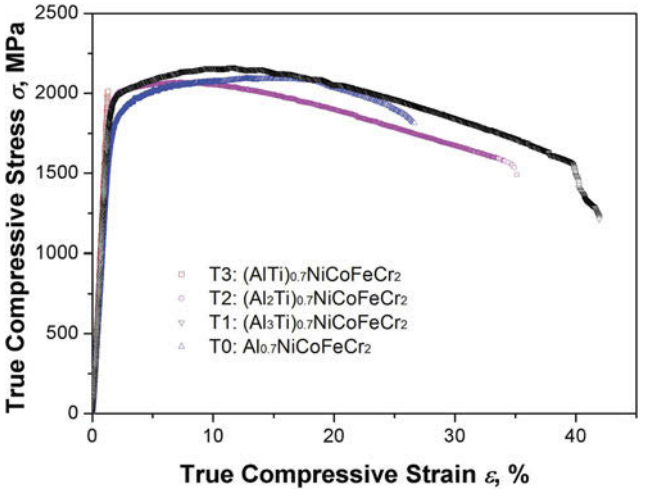

FIG. 7. True compressive stress–strain curves of the designed HEAs with different Ti contents.

and BCC phases in different regions using the SAED patterns [Figs. 4(b) and 4(c)]. It was found that the lattice constant of the BCC phase in the inner-dendrite (a_{BCC} = 0.2878 nm) is slightly larger than that in the interdendrite (a_{BCC} = 0.2866 nm), while the lattice constant of $L2_1$ in the inner-dendrite (a_{L21} = 0.5781 nm) is slightly smaller than that in the interdendrite (a_{L21} = 0.5792 nm). Thus, it must result in an increase in the lattice misfit from ε = 0.43% in the inner-dendrite to ε = 1.04% in the interdendrite. Apparently, it can be seen from the DF images [Figs. 4(b) and 4(c)] that the $L2_1$ nanoprecipitates in the inner-dendrites maintain cuboidal and gradually change into a plate-like shape in the interdendrites, which is in coincidence with the variation tendency of lattice misfits between BCC and $L2_1$ phases in these two regions. In principle, the equilibrium shape of coherent precipitates is determined by minimizing the sum of the elastic and interfacial energies, which is closely related to the lattice misfit (ε) and average particle size (r).[44–46] Actually, the lattice misfit will be dominant to the particle shape, when the particle size is larger than 40 nm.[18,19] Thereof, it can be concluded that the cuboidal shape of the $L2_1$ nanoprecipitates in the inner-dendrites of both T1 and T2 are a result of a moderate lattice misfit of ε = 0.4–0.6%. In comparison, a weave-like microstructure appears in the interdendrites of the T1 HEA, which resulted from a much larger lattice misfit of ε = 1.04% between the BCC and $L2_1$ phases, since it is difficult to control the shape of the precipitates in such a case.[44–46]

In our recent work, it is found that the higher strength caused by the cuboidal coherent microstructure of BCC and B2 phases in HEAs is mainly dependent on the coherent strengthening.[38] The yield strength increment, $\Delta\sigma_{CS}$, produced by coherent precipitation can be calculated with the following equation[18,19,47]:

$$\Delta\sigma_{cs} = M \times a_{\varepsilon} \times (G\varepsilon_c)^{3/2} \times (rf/0.5Gb)^{1/2} \quad ,$$

where M = 2.73 for the BCC structure (Taylor factor),[48] α_ε = 2.6 (a constant),[49] and $\varepsilon_c = 2\varepsilon/3$,[49] the constrained lattice misfit. G is the shear modulus of the matrix; b is the Burgers vector; r is the average particle size (the diameter of the spherical particle or the length of the cuboidal particle) and f is the volume fraction of the precipitates. According to this equation, the strength increments of $\Delta\sigma_{CS}$ of T0, T1, and T2 HEAs are calculated, being $\Delta\sigma_{CS}$ = 2041 MPa for T0, $\Delta\sigma_{CS}$ = 2070 MPa for T1, and $\Delta\sigma_{CS}$ = 2491 MPa for T2. Parameters used for calculations are G = 83 GPa (for α-Fe),[50] and Burgers vectors b = 0.2473 nm for T0, 0.2490 nm for T1, and 0.2505 nm for T2. And other parameters are listed in Table I. The compressive yield strengths of these three HEAs measured from the experiments are close to those calculated values according to the coherent strengthening. In fact, the mechanisms for precipitation strengthening are generally divided into two categories, Orowan bowing and particle shearing, which depends on the interactions between moving dislocations and precipitates. So it needs to be further studied for this HEA series through considering multiple factors, such as the antiphase boundary energy.

V. CONCLUSION

In the present work, a series of $(Al,Ti)_{0.7}NiCoFeCr_2$ HEAs with different Al/Ti ratios of 3/1, 2/1, and 1/1 were designed to investigate the effect of Ti substitution for Al on the cuboidal nanoprecipitates. The addition of Ti can change the phase constitutions of HEAs, especially the precipitated phase from the ordered B2-AlNi to a highly ordered $L2_1$-Ni_2AlTi on the BCC matrix. More importantly, a small amount addition of Ti (≤4.2 at.%, Al/Ti ratio ≥2/1) does not change the shape of nanoprecipitates in the inner-dendrites of HEAs, still maintaining the cuboidal $L2_1$ nanoparticles with a size of about 50–90 nm in the BCC matrix, which is attributed to the moderate lattice misfit (ε = 0.5–0.6%) between BCC and $L2_1$ phases. While a weave-like microstructure in the interdendrites of HEAs is resulted from a relatively larger lattice misfit of about 1.0%. HEAs with such a coherent microstructure exhibit the high compressive yield strength of about 1700–1800 MPa. Further increasing the Ti content up to 6.25 at.% (Al/Ti ratio of 1/1), the σ phase, not the BCC structure, is dominant as the matrix of the alloy, as a result of heavy brittleness.

ACKNOWLEDGMENTS

It was supported by the National Key Research and Development Plan (2017YFB0702400), the

International Science & Technology Cooperation Program of China (2015DFR60370), and the National Magnetic Confinement Fusion Energy Research Project (2015GB121004).

REFERENCES

1. J.W. Yeh, S.K. Chen, S.J. Lin, J.Y. Gan, T.S. Chin, T.T. Shun, C.H. Tsau, and S.Y. Chang: Nanostructured high-entropy alloys with multiple principal elements: Novel alloy design concepts and outcomes. *Adv. Eng. Mater.* **6**, 299 (2004).
2. Y. Zhang, T.T. Zuo, Z. Tang, M.C. Gao, K.A. Dahmen, P.K. Liaw, and Z.P. Lu: Microstructures and properties of high-entropy alloys. *Prog. Mater. Sci.* **61**, 1 (2014).
3. D.B. Miracle and O.N. Senkov: A critical review of high entropy alloys and related concepts. *Acta Mater.* **122**, 448 (2016).
4. O.N. Senkov, J.D. Miller, D.B. Miracle, and C. Woodward: Accelerated exploration of multi-principal element alloys with solid solution phases. *Nat. Commun.* **6**, 6529 (2015).
5. M.C. Gao, P.K. Liaw, J.W. Yeh, and Y. Zhang: *High-entropy Alloys: Fundamentals and Applications*, 1st ed. (Springer International Publishing, Cham, 2016).
6. B. Gludovatz, A. Hohenwarter, D. Catoor, E.H. Chang, E.P. George, and R.O. Ritchie: A fracture-resistant high-entropy alloy for cryogenic applications. *Science* **345**, 1153 (2014).
7. F. Otto, A. Dlouhy, C. Somsen, H. Bei, G. Eggeler, and E.P. George: The influences of temperature and microstructure on the tensile properties of a CoCrFeMnNi high-entropy alloy. *Acta Mater.* **61**, 5743 (2013).
8. O.N. Senkov, G.B. Wilks, J.M. Scott, and D.B. Miracle: Mechanical properties of $Nb_{25}Mo_{25}Ta_{25}W_{25}$ and $V_{20}Nb_{20}Mo_{20}Ta_{20}W_{20}$ refractory high entropy alloys. *Intermetallics* **19**, 698 (2011).
9. O.N. Senkov, J.M. Scott, S.V. Senkova, D.B. Miracle, and C.F. Woodward: Microstructure and room temperature properties of a high-entropy TaNbHfZrTi alloy. *J. Alloys Compd.* **509**, 6043 (2011).
10. O.N. Senkov, S.V. Senkova, and C.F. Woodward: Effect of aluminum on the microstructure and properties of two refractory high-entropy alloys. *Acta Mater.* **68**, 214 (2014).
11. K.M. Youssef, A.J. Zaddach, C. Niu, D.L. Lrving, and C.C. Koch: A novel low-density, high-hardness, high-entropy alloy with close-packed single-phase nanocrystalline structures. *Mater. Res. Lett.* **3**, 95 (2015).
12. A. Takeuchi, K. Amiya, T. Wada, K. Yubuta, and W. Zhang: High-entropy alloys with a hexagonal close-packed structure designed by equi-atomic alloy strategy and binary phase diagrams. *JOM* **66**, 1984 (2014).
13. M.C. Gao, B. Zhang, S.M. Guo, J.W. Qiao, and J.A. Hawk: High-entropy alloys in hexagonal close packed structure. *Metall. Mater. Trans. A* **47**, 3322 (2016).
14. M.A. Hemphill, T. Yuan, G.Y. Wang, J.W. Yeh, C.W. Tsai, A. Chuang, and P.K. Liaw: Fatigue behavior of high entropy alloys. *Acta Mater.* **60**, 5723 (2012).
15. J.Y. He, H. Wang, H.L. Huang, X.D. Xu, M.W. Chen, Y. Wu, X.J. Liu, T.G. Nieh, K. An, and Z.P. Lu: A precipitation-hardened high-entropy alloy with outstanding tensile properties. *Acta Mater.* **102**, 187 (2016).
16. D.Y. Li, C.X. Li, T. Feng, Y.D. Zhang, G. Shang, J.J. Lewandowski, P.K. Liaw, and Y. Zhang: High-entropy $Al_{0.3}CoCrFeNi$ alloy fibers with high tensile strength and ductility at ambient and cryogenic temperatures. *Acta Mater.* **123**, 285 (2017).
17. S.Z. Niu, H.C. Kou, T. Guo, Y. Zhang, J. Wang, and J.S. Li: Strengthening of nanoprecipitations in an annealed $Al_{0.5}CoCrFeNi$ high entropy alloy. *Mater. Sci. Eng., A* **671**, 82 (2016).
18. A.J. Ardell: Precipitation hardening. *Metall. Trans. A* **16**, 2131 (1985).
19. A. Argon: *Strengthening Mechanisms in Crystal Plasticity* (Oxford University Press, Oxford, U.K., 2007).
20. P. Caron and T. Khan: Evolution of Ni-based superalloys for single crystal gas turbine blade applications. *Aerosp. Sci. Technol* **3**, 513 (1999).
21. J.V. Goerler, I. Lopez-galilea, L.M. Roncery, O. Shchyglo, W. Theisen, and I. Steinbachet: Topological phase inversion after long-term thermal exposure of nickel-base superalloys: Experiment and phase-field simulation. *Acta Mater.* **124**, 151 (2017).
22. J.Y. He, H. Wang, Y. Wu, X.J. Liu, H.H. Mao, T.G. Nieh, and Z.P. Lu: Precipitation behavior and its effects on tensile properties of FeCoNiCr high-entropy alloys. *Intermetallics* **79**, 41 (2016).
23. Q. Wang, Y. Ma, B.B. Jiang, X.N. Li, Y. Shi, C. Dong, and P.K. Liaw: A cuboidal B2 nanoprecipitation-enhanced body-centered-cubic alloy $Al_{0.7}CoCrFe_2Ni$ with prominent tensile properties. *Scr. Mater.* **120**, 85 (2016).
24. Y. Ma, B.B. Jiang, C.L. Li, C. Dong, P.K. Liaw, F. Xu, and L.X. Sun: The BCC/B2 morphologies in $Al_xNiCoFeCr$ high-entropy alloys. *Metals* **7**, 57 (2017).
25. W.R. Wang, W.L. Wang, and J.W. Yeh: Phases, microstructure and mechanical properties of $Al_xCoCrFeNi$ high-entropy alloys at elevated temperatures. *J. Alloys Compd.* **589**, 143 (2014).
26. R.R. Chen, G. Qin, H.T. Zheng, L. Wang, Y.Q. Su, Y.L. Chiu, H.S. Ding, J.J. Guo, and H.Z. Fu: Composition design of high entropy alloys using the valence electron concentration to balance strength and ductility. *Acta Mater.* **144**, 129 (2018).
27. Y.S. Na, K.R. Lim, H.J. Chang, and J. Kim: Effect of trace additions of Ti on the microstructure of AlCoCrFeNi-based high entropy alloy. *Sci. Adv. Mater.* **8**, 1984 (2016).
28. Y.J. Zhou, Y. Zhang, Y.L. Wang, and G.L. Chen: Solid solution alloys of $AlCoCrFeNiTi_x$ with excellent room-temperature mechanical properties. *Appl. Phys. Lett.* **90**, 253 (2007).
29. K.B. Zhang, Z.Y. Fu, J.Y. Zhang, W.M. Wang, H. Wang, Y.C. Wang, Q.J. Zhang, and J. Shi: Microstructure and mechanical properties of $CoCrFeNiTiAl_x$, high-entropy alloys. *Mater. Sci. Eng., A* **508**, 214 (2009).
30. B. Gwalani, A.V. Ayyagari, D. Choudhuri, T. Scharf, S. Mukherjee, M. Gibson, and R. Banerjee: Microstructure and wear resistance of an intermetallic-based $Al_{0.25}Ti_{0.75}CoCrFeNi$ high entropy alloy. *Mater. Chem. Phys.* **210**, 197 (2018).
31. T.T. Shun, L.Y. Chang, and M.H. Shiu: Microstructure and mechanical properties of multiprincipal component $CoCrFeNiMo_x$ alloys. *Mater. Sci. Eng., A* **556**, 170 (2012).
32. S.M. Zhu, S.C. Tjong, and J.K.L. Lai: Creep behavior of a β′ (NiAl) precipitation strengthened ferritic Fe–Cr–Ni–Al alloy. *Acta Mater.* **46**, 2969 (1998).
33. C. Stallybrass, A. Schneider, and G. Sauthoff: The strengthening effect of (Ni,Fe)Al precipitates on the mechanical properties at high temperatures of ferritic Fe–Al–Ni–Cr alloys. *Intermetallics* **13**, 1263 (2005).
34. G. Song, Z. Sun, L. Li, X. Xu, M. Rawlings, C.H. Liebscher, B. Clausen, J. Poplawsky, D.N. Leonard, S.Y. Huang, Z.K. Teng, C.T. Liu, M.D. Asta, Y.F. Gao, D.C. Dunand, G. Ghosh, M.W. Chen, M.E. Fine, and P.K. Liaw: Ferritic alloys with extreme creep resistance via coherent hierarchical precipitates. *Sci. Rep.* **5**, 16327 (2015).
35. G. Song, Z. Sun, J.D. Poplawsky, Y. Gao, and P.K. Liaw: Microstructural evolution of single Ni_2TiAl or hierarchical NiAl/Ni_2TiAl precipitates in Fe–Ni–Al–Cr–Ti ferritic alloys during thermal treatment for elevated-temperature applications. *Acta Mater.* **127**, 1 (2017).
36. M.J.S. Rawlings, C.H. Liebscher, M. Asta, and D.C. Dunand: Effect of titanium additions upon microstructure and properties of

precipitation-strengthened Fe–Ni–Al–Cr ferritic alloys. *Acta Mater.* **128**, 103 (2017).
37. R. Feng, M.C. Gao, C. Zhang, W. Guo, J.D. Poplawsky, F. Zhang, J.A. Hawk, J.C. Neuefeind, Y. Ren, and P.K. Liaw: Phase stability and transformation in a light-weight high-entropy. *Acta Mater.* **146**, 280 (2018).
38. Y. Ma, Q. Wang, B.B. Jiang, C.L. Li, J.M. Hao, X.N. Li, C. Dong, and T.G. Nieh: Controlled formation of coherent cuboidal nano-precipitates in body-centered cubic high-entropy alloys based on $Al_2(Ni,Co,Fe,Cr)_{14}$ compositions. *Acta Mater.* **147**, 213 (2018).
39. C. Pang, B.B. Jiang, Y. Shi, Q. Wang, and C. Dong: Cluster-plus-glue-atom model and universal composition formulas [cluster] $(\text{glue atom})_x$ for BCC solid solution alloys. *J. Alloys Compd.* **652**, 63 (2015).
40. A. Takeuchi and A. Inoue: Calculations of mixing enthalpy and mismatch entropy for ternary amorphous alloys. *Mater. Trans., JIM* **41**, 1372 (2007).
41. D.B. Cullity and S.R. Stock: *Elements of X-Ray Diffraction*, 3rd ed. (Prentice Hall, Englewood, 2001).
42. R.S. Polvani, W.S. Tzeng, and P.R. Strutt: High temperature creep in a semi-coherent NiAl–Ni_2AlTi alloy. *Metall. Trans. A* **7**, 33 (1976).
43. P.R. Strutt, R.S. Polvani, and J.C. Ingram: Creep behavior of the heusler type structure alloy Ni_2AlTi. *Metall. Trans. A* **7**, 23 (1976).
44. P.W. Voorhees, G.B. Mcfadden, and W.C. Johnson: On the morphological development of second-phase particles in elastically-stressed solids. *Acta Metall. Mater.* **40**, 2979 (1992).
45. P. Fratzl, O. Penrose, and J.L. Lebowitz: Modeling of phase separation in alloys with coherent elastic misfit. *J. Stat. Phys.* **95**, 1429 (1999).
46. M.E. Thompson, C.S. Su, and P.W. Voorhees: The equilibrium shape of a misfitting precipitate. *Acta Metall. Mater.* **42**, 2107 (1994).
47. E. Nembach: Precipitation hardening caused by a difference in shear modulus between particle and matrix. *Phys. Status Solidi* **78**, 571 (1983).
48. W.F. Hosford: *Mechanical Behavior of Materials*, 1st ed. (Cambridge University Press, Cambridge, 2005).
49. B. Jansson and A. Melander: On the critical resolved shear stress from misfitting particles. *Scr. Metall.* **12**, 497 (1978).
50. ASM International Handbook Committee: *Properties and Selection: Irons, Steels and High Performance Alloys*, 2nd ed. (ASM International, Ohio, 1993).